Rotational Intergrowth

DOI: 10.1002/anie.201402024

On the Rotational Intergrowth of Hierarchical FAU/EMT Zeolites**

*Maryam Khaleel, Andrew J. Wagner, K. Andre Mkhoyan, and Michael Tsapatsis**

***Abstract:** A structural study of a hierarchical zeolite X, which is similar to the one first synthesized by Inayat et al.,[12] was performed using transmission electron microscopy imaging and diffraction. Evidence is provided, by comparison to simulations, that this material is an intergrowth of FAU and EMT and a conceptual model is presented for the growth of the FAU material with a small fraction of EMT in an atypical morphology of assembled sheets with well-defined intersection angles.*

Hierarchical zeolites contain highly interconnected networks of zeolitic micropores combined with meso- and/or macropores.[1–3] Interest in these materials stems from the higher reaction rates,[4,5] improved selectivity,[6,7] resistance to deactivation,[7–9] and novel adsorption behavior[10] that they exhibit in comparison to the typical zeolites that have only micropores. Among the synthesis approaches,[11] the repetitive branching by rotational intergrowth[5,12,13] holds promise for industrial implementation due to its simplicity (one-step synthesis) and lower cost (simple structure-directing agents or additives) compared to hard[14] and dual-soft templating[15] approaches.

Single-unit-cell nanosheets of the commercially important zeolite framework MFI can be intergrown orthogonally to each other to form a self-pillared hierarchical zeolite.[5,10] It has been proposed that connectivity at the intersections of the nanosheets is achieved by a higher-symmetry-related zeolite (MEL) acting as a 4-fold symmetric connector. Although definite proof (e.g., by imaging of these intersections) has not yet been presented, this connectivity provides a conceptual framework for constructing hierarchical zeolites by combining two materials, which can intergrow epitaxially, one with a lower symmetry (nanosheet) than the other (connector).

An analogous arrangement of faujasite nanosheets has been reported as a type X zeolite (Si/Al < 1.5).[12] The house-of-cards nanosheet structure combines faujasite micropores (0.74 nm) with mesopores (ca. 7 nm), which are located within the sheets (sheet thickness of ~ 100–200 nm), and macropores (ca. 200 nm) resulting from the intersection of the sheets. However, a plausible scenario for the process of branching was not presented so far. Understanding the branching mechanisms may allow controlling the nanosheet thickness, branching frequency, and other structural characteristics and here we attempt to provide such understanding. We demonstrate that the hierarchically branched faujasite mainly consists of FAU, but also contains a small amount of EMT, which plays a crucial role in directing the growth of the predominant FAU material in an atypical morphology of interpenetrating sheets with well-defined intersection angles of 70.5°. We also demonstrate that even though the growth instability, which causes branching, is caused by EMT, the connection between the nanosheets is attributed to FAU (i.e. EMT does not act as a connector).

The morphology reported by Inayat et al.[12] was confirmed using scanning electron microscopy (SEM) (Figure 1 a). It should be noted that in this case a homologous surfactant with two additional carbon atoms in the alkyl chain (3-(trimethoxysilyl) propyl octadecyldimethyl ammonium chloride, TPOAC) was used to form the hierarchical particles (TPOAC-hierarchical-faujasite = T-H-faujasite) (see the Supporting Information, SI, Section S1). Characterization by SEM, X-ray diffraction (XRD), porosimetry and nuclear magnetic resonance (NMR) of T-H-faujasite and comparison with conventional FAU (C-FAU) obtained in the absence of the surfactant, are presented in the Supporting Information. As shown in Figure 1 a, the intergrown nanosheets in T-H-faujasite form a skeletal cuboctahedron, such that from one direction a triangular assembly of sheets with 3-fold symmetry is observed (Figure 1 b) (corresponding to a triangular face in a cuboctahedron), and another direction shows a square assembly of sheets with a 4-fold symmetry (corresponding to a square face in a cuboctahedron). The cuboctahedron is a habit of cubic crystals as shown in Figure 1 c. The arrangement of T-H-faujasite sheets into this cuboctahedral skeletal arrangement can be easily visualized by the assembly of four hexagonal plates ($\equiv$ 4 {111} planes) with interpenetration angles of 70.5° and 109.5° between any two plates (Figure 1 d).

A confirmation that the thin dimension of the nanosheets coincides with the $< 111 >_{\mathrm{cubic}}$ of faujasite is shown in Figure 2. By sonicating T-H-faujasite in ethanol for a few minutes, some sheets get dislodged from the particles. Fig-

---

[*] M. Khaleel, A. J. Wagner, Prof. K. A. Mkhoyan, Prof. M. Tsapatsis
Department of Chemical Engineering and Materials Science
University of Minnesota
421 Washington Ave SE, Minneapolis, MN 55455 (USA)
E-mail: tsapatsis@umn.edu

[**] Support for this work was provided by ADMIRE (Abu Dhabi–Minnesota Institute for Research Excellence) and the NSF (Emerging Frontiers in Research and Innovation 0937706). Part of this work was conducted at the University of Minnesota Characterization Facility, which receives partial support from the NSF through the NNIN program. Computing resources were provided by the Minnesota Supercomputing Institute. M.K. acknowledges support from ADNOC (Abu Dhabi National Oil Company). We thank N. Rangnekar, Dr. S. Hwang (Caltech), and R. Knurr for performing AFM, solid-state NMR and ICP-OES, respectively, and Dr. A. Mittal, Dr. J. Myers, and Prof. H. Gies (RUB) for helpful discussions. Author contributions: M.K. performed materials synthesis and characterization and analyzed and interpreted all experiments. M.T. conceived and directed the project. M.K. and M.T. produced the manuscript and developed the conceptual model of morphology development. A.J.W. and K.A.M. performed and analyzed the STEM-EDX experiments shown in Figure 5.

Supporting information for this article is available on the WWW under http://dx.doi.org/10.1002/anie.201402024.

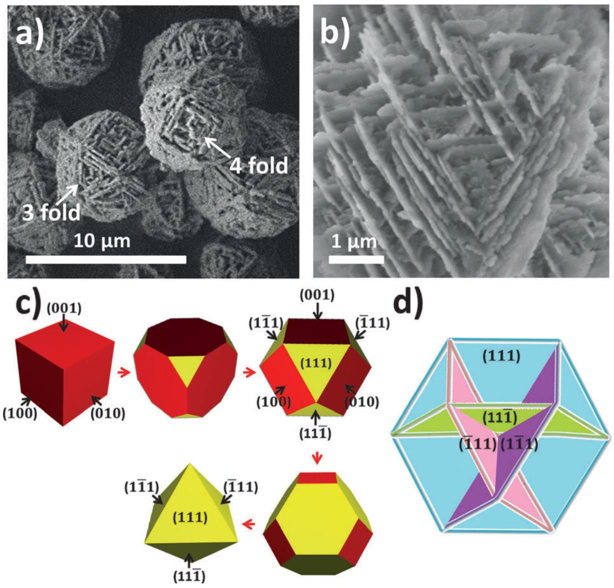

Figure 1. a) SEM image showing a view of the cuboctahedral skeletal arrangement of sheets in T-H-faujasite (3-fold and 4-fold symmetries in sheet arrangements are evident). b) SEM image highlighting the triangular assembly of T-H-faujasite sheets with 3-fold symmetry (corresponding to a triangular face in a cuboctahedron). c) Evolution of the cubic crystal habit from cube to octahedron (produced using Stella4D), {111} and {100} planes are labelled. d) Assembly of four hexagonal (111) plates with interpenetration angle of 70.5° or 109.5° between any two plates resulting in a cuboctahedral skeletal arrangement exhibiting 3-fold and 4-fold symmetric arrangement of plates.

ure 2a shows a high-resolution transmission electron microscopy (TEM) image [inset: fast fourier transform (FFT)] of such a sheet with a hexagonal symmetry, indicating that the thin dimension of the sheet coincides with $<111>_{\text{cubic}}$. In agreement with Inayat et al.,[12] mesoporosity is evident within the sheets (see arrows in Figure 2a). Figure 2c shows electron diffraction from another sheet with a hexagonal projection (Figure 2b). The electron diffraction pattern shows that the sheet is single-crystalline and has a hexagonal symmetry showing a hexagonal array of more intense spots, marked with A, which index according to the FAU $<111>$ zone axis and intervening weaker spots, marked with B, which index according to the EMT $<0001>$ zone axis. This confirms the conclusion drawn from high-resolution imaging that the thin dimension of the sheets coincides with $<111>_{\text{cubic}}$ and provides evidence for the possible presence of EMT. The relationship between FAU and EMT structures and their intergrowth is reviewed in the Supporting Information (Section S2.2). The fact that the intensities of the reflections marked by B are weak when compared to the A reflections, indicates that the sheet is not completely recurrently faulted.[16]

As shown by electron diffraction simulations (SI, Section S2.3), the reflections marked with B in Figure 2a,c can arise from regions of EMT intergrowing with FAU (Figure S6).[16] They can also arise from an incomplete cubic stacking sequence of faujasite layers for thin FAU sheets in the absence of EMT (Figure S7). Below we will argue in favor of the former.

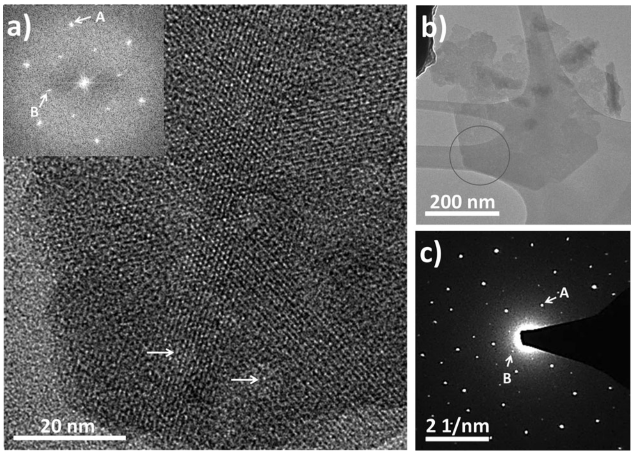

Figure 2. a) High-resolution TEM image showing a crystalline mesoporous sheet dislodged by sonication of T-H-faujasite in ethanol (mesopores are indicated by arrows) and inset FFT showing hexagonal symmetry. b) Low-magnification TEM image of a hexagonal sheet dislodged by sonication of T-H-faujasite in ethanol. c) Electron diffraction pattern of a selected area from the part of the sheet marked in (b). The reflections marked with A index according to the FAU $<111>$ zone axis and those marked with B index according to the EMT $<0001>$ zone axis. See the Supporting Information (Figure S6) for electron diffraction pattern indexing.

EMT domains in T-H-faujasite were observed both from the direct examination of thin sheets dislodged by sonication and from thin sections prepared by microtomy of T-H-faujasite particles embedded in polybed 812 (Figure 3). The TEM images show single faults and EMT extending for up to two unit cells along $<0001>$ and up to 20 nm in the directions perpendicular to $<0001>$. Region II marked in Figure 3a is a FAU domain and region III is a faulted domain indicating that EMT domains are interrupted and enclosed by FAU domains and/or amorphous regions or mesopores. Amorphous regions, visible in Figure 3b, could be partly responsible for the lower microporosity of T-H-faujasite compared to that of C-FAU, measured by Ar adsorption (see SI, Figure S4).

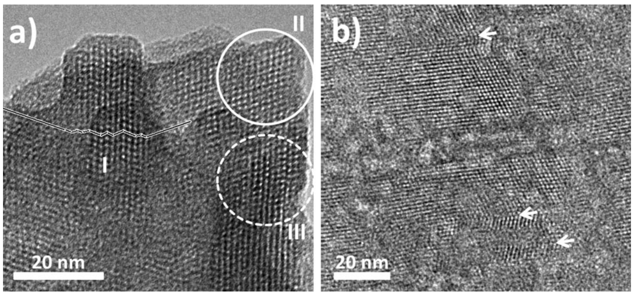

Figure 3. Bright-field TEM images showing a) faulting in a sheet dislodged by sonication of T-H-faujasite in ethanol (region I shows excessive faulting and regions II (FAU) and III (faulted) show that EMT domains are enclosed by FAU domains) and b) faulting in a sheet observed from thin microtomed section of T-H-faujasite embedded in polybed 812 (faults are marked by arrows).

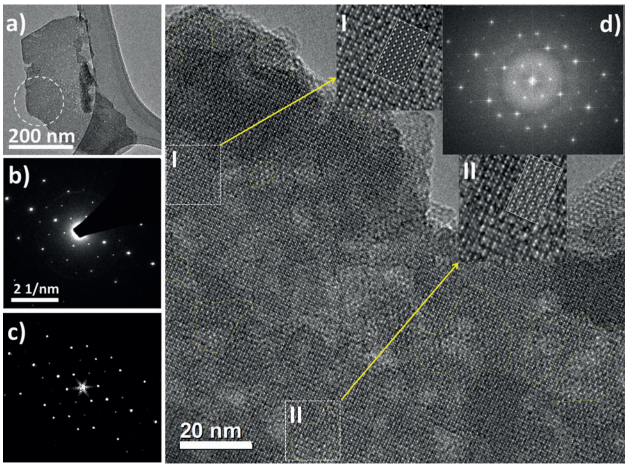

Figure 4. a) Low-magnification TEM image of a hexagonal sheet dislodged by sonication of T-H-faujasite in ethanol. b) Electron diffraction pattern of a selected area from the part of the sheet marked in (a). c) Simulated electron diffraction pattern from the $[323]_{cubic}$ zone axis for FAU, mirror FAU (rotated 60° around $[111]_{cubic}$ with respect to FAU aligned along $[323]_{cubic}$), and EMT. d) The $[323]_{cubic}$ high-resolution TEM image of a sheet (inset FFT) with the FAU/EMT domains marked and magnified regions I (FAU) and II (FAU/EMT) superimposed by simulated $[323]_{cubic}$ high-resolution images.

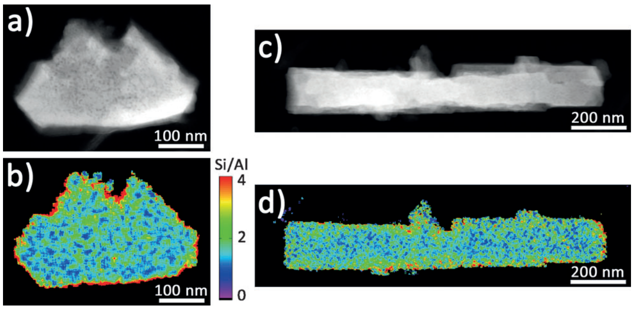

Figure 5. HAADF-STEM image and STEM-EDX Si/Al net count heat map of the top (a and b, respectively) and side views (c and d, respectively) of two different sheets. The color code bar on the right of the heat maps indicates the colors for a Si/Al ratio range from 0 to 4.

Additional confirmation of the presence of EMT domains (ca. 20 nm) within the sheets is obtained by electron diffraction and imaging along the $[323]_{cubic}$ zone axis (Figure 4). The diffraction pattern (Figure 4b) taken from the part of the dislodged sheet marked in Figure 4a shows reflections from the $[323]_{cubic}$ zone axis for FAU, mirror FAU (rotated 60° around $[111]_{cubic}$ with respect to FAU aligned along the $[323]_{cubic}$), and EMT. This is shown by the simulated diffraction pattern in Figure 4c (Figure S8). The same pattern of Figure 4b and c was also observed by FFT from high resolution imaging along the $[323]_{cubic}$ zone axis (Figure 4d and FFT inset).

The high-resolution image motif along the $[323]_{cubic}$ zone axis can also be used to distinguish FAU-only and FAU/EMT domains in a sheet. Down this zone axis, the projection of FAU shows a rectangular pattern while that of FAU/EMT shows a centered pattern with larger features (see Figure S9). Figure 4d shows the experimental TEM image marking representative FAU/EMT domains as determined by the [323] motif. Magnified views of regions I (FAU-only) and II (FAU/EMT) are presented and superimposed by the simulated [323] high-resolution images for FAU and FAU/EMT, respectively. This interpretation is also supported by image filtering, in which the removal of the EMT reflections from the FFT returns a high-resolution image without large, centered features (Figure S10). The $[323]_{cubic}$ view is in agreement with the $[111]_{cubic}$ view. In addition, it has the advantage of revealing the small portions of included EMT domains in the predominant FAU matrix.

Scanning transmission electron microscopy (STEM) analysis was performed to identify variations in the Si/Al ratio across the nanosheets. Figure 5 shows the high-angle annular dark-field (HAADF) STEM images and the STEM energy-dispersive X-ray (STEM-EDX) Si/Al net count heat maps of sheets dislodged by sonication in ethanol. The HAADF images show spots with dark contrast corresponding to the mesopores of about 5 nm size. Due to beam damage, the zeolite particles lose their crystallinity. The loss of crystallinity apparently densifies the particles and some shrinkage is evident by observing a sequence of TEM images at different stages of electron beam exposure (net doses as high as 10^6 electrons per nm^2). However, this damage appears to be local, as there are no apparent changes in the contrast attributed to the mesopores with increased electron beam exposure. Therefore, we believe that despite the electron beam damage, the Si/Al ratio determined by EDX is representative of that in the undamaged sample. Unlike silicon and aluminum, sodium migrates fast out of the sample and is found in the vicinity of the zeolite particles on the copper grid.

The EDX Si/Al net count heat maps show that, on a 10 nm scale, there is a factor of 2.5 variation in Si/Al across the sheets. At this level of resolution, we find no evident correlation of the Si/Al ratio with morphological features like surface steps and pores. Moreover, due to the beam damage, we are not able to conclude if the differences in Si/Al are associated with the FAU/EMT versus FAU-only domains discussed in Figure 4. This should be the subject of further investigations.

The edges of the sheets show an apparent higher Si/Al ratio compared to the bulk. This is believed to be an artifact resulting from the low counts per pixel at the thin edges. It arises from the small dwell time needed to limit beam damage coupled with the reduced interaction volume at the thin particle edges. This was concluded by careful examination of the number of X-ray counts and is supported by X-ray photoelectron spectroscopy (XPS) data, which do not show a Si-rich surface for the sheets (the Si/Al ratio on the surface of the zeolite particles was determined by XPS to be 1.7). The average Si/Al ratios obtained from EDX measurements for both sheets (excluding edges) is 1.6, which, considering that we did not use a calibration standard, is in good agreement with the Si/Al ratio determined by inductively coupled plasma optical emission spectroscopy (ICP-OES) (1.4) and SEM-EDX (1.3).

The results presented above show that T-H-faujasite: 1) at the particle level has a cuboctahedron morphology consistent with cubic FAU; 2) each cuboctahedron particle consists of a skeletal arrangement of nanosheets interpenetrating at 70.5° or 109.5°; 3) each nanosheet is thin along the $< 111 >_{\text{cubic}}$ axis, and is predominantly composed of FAU, with EMT present in small isolated domains that do not give rise to XRD peaks. The presence of these hardly detectable EMT domains appears to be the necessary ingredient for the formation of T-H-faujasite. We will argue in the following that EMT not only directs the formation of anisotropic nanosheets but also (although it does not act as a connector between the nanosheets) creates the growth instability leading to branching.

According to the Hartman–Perdok theory, FAU $\{111\}$ faces are classified as "F faces" (flat and slow growing faces), because they have three coplanar periodic bond chains (PBCs) within a slice of the thickness d_{111}.[17] The perpendicular $< 111 >$ directions to these faces are the directions along which the faujasite layers stack and can fault. Intergrowths are possible because the (111) plane in FAU is identical to the (0001) plane in EMT. For a pure FAU phase, the growth is isotropic. However, if instead of inversion, a mirror plane (fault) forms along one of the four faujasite sheet stacking directions, a local hexagonal (EMT) structure is created supporting anisotropic growth. For EMT, the in-plane growth perpendicular to $< 0001 >$ has been reported to be 15 times faster than the growth along $< 0001 >$ and is reflected in the hexagonal platelet morphology of EMT.[18] The fast in-plane growth of EMT is anticipated by the Hartman–Perdok PBC theory, which states that the dimension of a crystal along a particular direction is proportional to the bonding strength along that direction. Each sodalite cage has three double-6 member ring connections along a (111) plane and only one connection either to the faujasite layer above or below. Less bonding along the $< 111 >_{\text{cubic}}$ and the $< 0001 >_{\text{hex}}$ axes favors in-plane growth. This is also anticipated by the Bravais–Friedel–Donnay–Harker (BFDH) theory, because the $< 0001 >$ spacing in EMT is the largest and therefore the growth along this direction is expected to be the slowest. According to these arguments based on PBC and BFDH theories and prior experimental evidence, the EMT domains are necessary for the nanosheet morphology to develop. The small size of EMT domains is apparently a result of the simultaneous multiple nucleation of FAU and EMT on $\{111\}$ faces in a growth regime favoring 2D nucleation and slower (with respect to nucleation) in-plane propagation such that as growth progresses, EMT gets overgrown by the predominant FAU (Figure S11). It is likely that the organosilane surfactant used for the T-H-faujasite synthesis as a mesoporogen also acts, upon incorporation at a growth front, to retard the propagation of the nucleated islands.

This model is supported by atomic force microscopy (AFM) measurements on dislodged T-H-faujasite sheets (deposited on a silicon wafer) that show the presence of islands with lateral dimensions and heights as small as approximately 20 nm and 1 nm, respectively (Figure S12). Steps with heights corresponding to one (1.42 nm) and two (2.85 nm) faujasite layers were observed frequently, but not exclusively, on these surfaces. This surface structure might not be indicative of the surface structure under growth conditions, but it is consistent with the TEM observations and the proposed growth model.

The remaining question is how branching happens. If growth proceeds by nucleating FAU and EMT on a single (111) face, a fast propagation in-plane will lead to sheets. A different event has to happen at the branching points. We argue that EMT island nucleation at the edge of a nanosheet is responsible for branching. EMT nucleation is a random event and happens on all $\{111\}$ faces. If EMT nucleates on a vicinal $\{111\}$ plane near the edge of the basal plane, it can extend along its fast growing direction before being overgrown by FAU domains. Figure 6a shows an example, in which EMT nucleation at the edge of a plate (sheet 1), on its (111) and $(11\bar{1})$ faces, is followed by branching to form sheet 2. Further growth leads to sheet interpenetration. Other possible scenarios are presented in Figure S13 and different interpenetration possibilities are presented in Figure S14. It should be noted that sheet 2 does not necessarily contact sheet 1 throughout its plane dimensions. This is supported by Figure 6b, which shows out-growing sheets that are laterally much smaller than the basal sheet in the image plane.

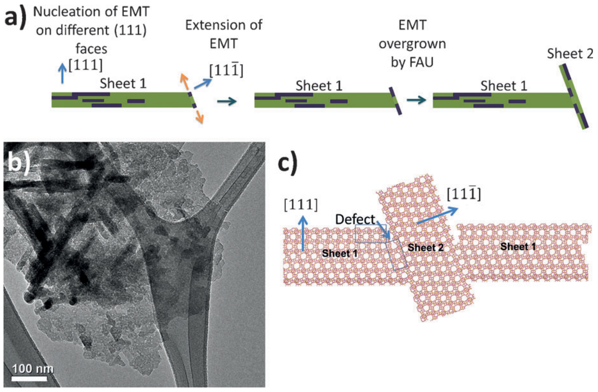

Figure 6. Illustration of the branching mechanism in T-H-faujasite. a) Nucleation of EMT close to the edge of sheet 1 on (111) and $(11\bar{1})$ followed by its extension along its fast growing direction before being overgrown by FAU domains leads to branching of sheet 2. b) TEM image highlighting the triangular assembly of T-H-faujasite sheets with 3-fold symmetry (corresponding to a triangular face in a cuboctahedron; the interconnected sheets were dislodged by sonicating T-H-faujasite in ethanol. c) Structural model showing defect formation when the EMT domains on (111) and $(11\bar{1})$ meet, because EMT cannot coherently bond at 70.5°.

Sheet 1 in Figure 6a slowly grows perpendicular to its plane because sheet 2 deprives it of nutrients as the latter extends along its plane and develops as a sheet. This allows the structure to branch and grow in a skeletal morphology before the voids are filled at long synthesis times and an octahedral morphology develops (Figure S15). Sheet 2 eventually thickens and gets surrounded by FAU and branching can happen on this sheet as well. This process repeats itself in all four $< 111 >_{\text{cubic}}$ directions (Figure 1d), leading to the hierarchical open house-of-cards arrangement with a well-defined interpenetration angle of 70.5°. If EMT domains, which nucleated on two different neighboring {111} faces [e.g., (111) and $(11\bar{1})$], meet, a defect will form, because EMT cannot coherently bond at 70.5° (Figure 6c). Such a highly disrupted structure with a large number of defects has also been reported for ZSM-20 prepared using the tetraethylammonium cation, which also grows as interpenetrating plates,[18] but with less branching than observed for T-H-faujasite. According to the model, the connection between the sheets is FAU, which is cubic and can coherently connect at angles of 70.5°.

Our proposed conceptual growth model suggests that the random nucleation of small EMT islands, which are not detectable by XRD, on all {111} faces and under growth conditions far from equilibrium, which are characterized by a delicate interplay between surface nucleation, step propagation, and branching, lead to the repetitively branched morphology. This type of dendritic growth is analogous, yet distinct, to that observed in more common crystals including snowflakes. The latter, for example, form a hexagonal lattice that cannot coherently bond at 70.5° and so they branch only in-plane, thereby forming thin hexagonal plates at suitable conditions (Figure 7b).[19] Such branching, along the intrinsic directions of fast growth, occurs when the growth is fast in the beginning, but then switches to faceting when supersaturation drops, developing hexagonal plates.[19] T-H-faujasite appears to follow the same growth principle (Figure 7a), but since it is predominantly cubic, it can branch in four directions due to the growth instability introduced by EMT.

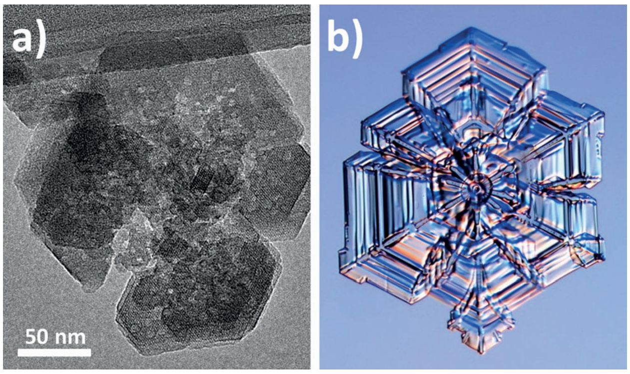

Figure 7. a) Low-magnification TEM image of a mesoporous Faujasite sheet dislodged by sonicating T-H-faujasite in ethanol. b) Snowflake (Reprinted with permission from reference [20]). Copyright 2006 by Kenneth Libbrecht.

This model for intergrowth is conceptually different from the model that was developed for the self-pillared pentasil (SPP).[5] Although both are based on polytypism, it was hypothesized for SPP that MFI sheets grow epitaxially from a higher symmetry MEL node that acts as a connector, whereas in the case of T-H-faujasite, the EMT islands intergrow with FAU to break up the cubic symmetry within a nanosheet. According to the proposed model, hierarchical faujasite consisting exclusively of single unit sheets cannot be made by this branching mechanism, because branching requires a certain thickness of FAU to be achieved first and rare EMT nucleation to take place at its edges. This, and the earlier work on MFI/MEL,[5] demonstrate that there is a direct link between the polytypes involved and the repetitive branching mechanism leading to the hierarchical structures. Once understood, this mechanism will set the stage of what is achievable in terms of characteristic diffusion length, mesopore size, and other characteristics. Similar investigations on other documented intergrowths (e.g. CHA/SOD[21] and ETS-10/ETS-4)[22] are desirable to establish possible branching mechanisms leading to hierarchical materials.

Received: February 2, 2014
Revised: June 12, 2014

Keywords: hierarchical structure · nanosheets · rotational intergrowth · zeolites · formation mechanism

[1] A. Corma, *Chem. Rev.* **1997**, *97*, 2373–2419.
[2] M. Davis, *Nature* **2002**, *417*, 813–821.
[3] W. Roth, P. Nachtigall, R. Morris, J. Čejka, *Chem. Rev.* **2014**, *114*, 4807–4837.
[4] S. van Donk, A. Broersma, O. Gijzeman, J. van Bokhoven, J. Bitter, K. de Jong, *J. Catal.* **2001**, *204*, 272–280.
[5] X. Zhang, D. Liu, D. Xu, S. Asahina, K. Cychosz, K. Agrawal, Y. Wahedi, A. Bhan, S. Hashimi, O. Terasaki, M. Thommes, M. Tsapatsis, *Science* **2012**, *336*, 1684–1687.
[6] C. Christensen, K. Johannsen, I. Schmidt, C. Christensen, *J. Am. Chem. Soc.* **2003**, *125*, 13370–13371.
[7] a) J. García-Martínez, M. Johnson, J. Valla, K. Li, J. Ying, *Catal. Sci. Technol.* **2012**, *2*, 987–994; b) J. Garcia-Martinez, K. Li, G. Krishnaiah, *Chem. Commun.* **2012**, *48*, 11841–11843.
[8] R. Srivastava, M. Choi, R. Ryoo, *Chem. Commun.* **2006**, 4489–4491.
[9] M. Choi, K. Na, J. Kim, Y. Sakamoto, O. Terasaki, R. Ryoo, *Nature* **2009**, *461*, 246–250.
[10] D. Xu, G. Swindlehurst, H. Wu, D. Olson, X. Zhang, M. Tsapatsis, *Adv. Funct. Mater.* **2014**, *24*, 201–208.
[11] a) R. Chal, C. Gerardin, M. Bulut, S. van Donk, *ChemCatChem* **2011**, *3*, 67–81; b) Y. Tao, H. Kanoh, L. Abrams, K. Kaneko, *Chem. Rev.* **2006**, *106*, 896–910; c) J. Pérez-Ramírez, C. Christensen, K. Egeblad, C. Christensen, J. Groen, *Chem. Soc. Rev.* **2008**, *37*, 2530–2542; d) J. Čejka, S. Mintova, *Catal. Rev.* **2007**, *49*, 457–509; e) W. Schmidt, *ChemCatChem* **2009**, *1*, 53–67; f) S. Lopez-Orozco, A. Inayat, A. Schwab, T. Selvam, W. Schwieger, *Adv. Funct. Mater.* **2011**, *23*, 2602–2615.
[12] A. Inayat, I. Knoke, E. Spiecker, W. Schwieger, *Angew. Chem.* **2012**, *124*, 1998–2002; *Angew. Chem. Int. Ed.* **2012**, *51*, 1962–1965.
[13] W. Chaikittisilp, Y. Suzuki, R. Mukti, T. Suzuki, K. Sugita, K. Itabashi, A. Shimojima, T. Okubo, *Angew. Chem.* **2013**, *125*, 3439–3443; *Angew. Chem. Int. Ed.* **2013**, *52*, 3355–3359.
[14] W. Fan, M. Snyder, S. Kumar, P.-S. Lee, W.-C. Yoo, A. McCormick, R. Penn, A. Stein, M. Tsapatsis, *Nat. Mater.* **2008**, *7*, 984–991.
[15] a) M. Choi, H. Cho, R. Srivastava, C. Venkatesan, D.-H. Choi, R. Ryoo, *Nat. Mater.* **2006**, *5*, 718–723; b) K. Cho, H. Cho, LC. de Menorval, R. Ryoo, *Chem. Mater.* **2009**, *21*, 5664–5673; c) G. Shanbhag, M. Choi, J. Kim, R. Ryoo, *J. Catal.* **2009**, *264*, 88–92.
[16] G. Millward, J. Thomas, S. Ramdas, M. Barlow, *Proceedings of the 6th International Zeolite Conference, Reno, USA, 10–15 July*

1983 (Eds.: D. Olson, A. Bisio), Butterworths, Guildford, **1984**, pp. 793 – 802.

[17] a) P. Hartman, W. Perdok, *Acta Crystallogr.* **1955**, *8*, 49; b) P. Hartman, W. Perdok, *Acta Crystallogr.* **1955**, *8*, 525.

[18] O. Terasaki, T. Ohsuna, V. Alfredsson, J. Bovin, D. Watanabe, S. Carr, M. Anderson, *Chem. Mater.* **1993**, *5*, 452 – 458.

[19] K. Libbrecht, *Rep. Prog. Phys.* **2005**, *68*, 855 – 895.

[20] K. Libbrecht, *Ken Libbrecht's Field Guide to Snowflakes*, Voyageur Press, Minnesota, **2006**.

[21] T. Wakihara, S. Yamakita, K. Iezumi, T. Okubo, *J. Am. Chem. Soc.* **2003**, *125*, 12388 – 12389.

[22] H.-K. Jeong, J. Krohn, K. Sujaoti, M. Tsapatsis, *J. Am. Chem. Soc.* **2002**, *124*, 12966 – 12968.